ELSEVIER

Anomaly subspace detection based on a multi-scale Markov random field model

Arnon Goldman, Israel Cohen*

Department of Electrical Engineering, Technion - Israel Institute of Technology, Technion City, Haifa 32000, Israel

Abstract

In this paper we introduce a multi-scale Gaussian Markov random field (GMRF) model and a corresponding anomaly subspace detection algorithm. Natural clutter images, often appear to have several periodical patterns of various period lengths. In such cases, the GMRF model may not sufficiently describe the clutter image. The proposed model is based on a multi-scale wavelet representation of the image, independent component analysis, and modeling each independent component as a GMRF. Anomaly detection is subsequently carried out by applying a matched subspace detector to the innovations process generated by the presumed model. The robustness of the proposed approach is demonstrated with application to automatic target detection in synthetic and real imagery. A quantitative performance analysis and experimental results demonstrate the advantage of the proposed method in comparison to competing methods.
© 2004 Elsevier B.V. All rights reserved.

Keywords: Anomaly detection; Object recognition; Pattern recognition; Image segmentation; Image texture analysis; Gaussian Markov random field; Multi-scale representation; Matched subspace detector

1. Introduction

During the last decade, there has been a remarkable progress in random field models and their applications. Random field modeling has been applied extensively to texture synthesis [3,5], image segmentation [15,20,24], and target detection [11,19]. Most random field models are based on the spatial interaction of pixels in local neighborhoods. The noncausal autoregressive (NCAR) model represents each pixel as a linear combination of pixels at nearby locations, and an additive white noise variable (innovations process). Chellappa and Kashyap [3,13] proposed an iterative estimation method and synthesis algorithm for the two-dimensional NCAR model. They illustrated the usefulness of the NCAR

*Corresponding author.

E-mail addresses: goldman@techunix.technion.ac.il (A. Goldman), icohen@ee.technion.ac.il (I. Cohen).

URL: http://www-sipl.technion.ac.il/~cisrael.

models for synthesis of textures resembling several real texture images, possessing the local replication attribute. The local replication attribute is an essential ingredient of many natural textures [3].

The Markov random field (MRF) model was first introduced by Lévi [16] in 1956. Woods [25] formulated the two-dimensional discrete MRF based on the continuous case given by Lévi. The discrete MRF model describes each pixel as a weighted sum of its neighboring pixels and a random variable which represents the innovations process. The difference between the MRF model and the NCAR model is that the innovations process is spatially correlated.

A more general form of random field models is the long correlation (LC) model proposed by Kashyap and Lapsa [14]. The LC models can be applied to images with a correlation structure which extends over large regions using only a few model parameters. These models have a limited practical use, due to the lack of an effective method for estimating the model parameters [2]. Eom [5] proposed an LC model with circular and elliptical correlation structure and a corresponding estimation algorithm. The LC model has the advantage of modeling diverse real textures with less than five model parameters. Three parameters are used for defining an isotropic LC model and the other two parameters are used for describing the linear transformation (elongation and rotation) performed to the model's coordinate system. Bennett and Khotanzad [2] developed a random field model and a corresponding estimation scheme, based on a generalized long correlation (GLC) model. They showed that the NCAR and the MRF models are special cases of this model.

Random field models were developed for describing natural clutter images. Man-made objects therefore appear anomalous with respect to the random field model which is used to represent the clutter. Anomaly detection methods exploit the anomalous appearance of such objects for their detection, but often make no a priori assumptions about the nature of the targets. Hazel [11] has developed an anomaly detection technique, which is based on Gaussian MRF (GMRF) modeling of the background in a multi-spectral image. A single hypothesis scheme is used for the detection of regions, which appear unlikely with respect to the probabilistic model of the background. A similar anomaly detection method was proposed by Bello [1] for the detection of anomalous complex image pixels, using the simultaneous autoregressive (SAR) model. A completely different approach for target detection is based on a matched signal detector (matched filter). The matched signal detector is employed when a typical signature of the target is available. In many detection problems, the information about the targets is a subspace in which the targets lie. In these applications, the matched signal detector is replaced by a matched subspace detector (MSD), a generalization of the matched filter, which was formulated by Scharf and Friedlander [21]. The MSD is used for detecting subspace signals in subspace interference and additive noise, using the principle of the generalized likelihood ratio test (GLRT) . A recent review of anomaly detection methods can be found in Karkou and Singh [17]. The survey includes different statistical approaches for image modeling, hypothesis testing and clustering. Most of the presented methods are driven by modeling data distributions and then calculating the likelihood of test data with respect to the estimated statistical models.

In many natural clutter images, scene elements often appear to have several periodical patterns, of various period lengths. In such cases, the above-mentioned random field models may not sufficiently fit the clutter image. Deviations of the clutter image from the random field model influence the detection performance by increasing the false alarm rate. Furthermore, in real detection problems, some a priori information about the targets is often available. Using this information for rejecting anomalies, which do not resemble targets, may improve the detection performance.

In previous papers, we proposed an iterative anomaly detection approach for cases where the background data is composed of a mixture of different textures [8,10]. A different approach is proposed in [9], where we first present a modified MSD for anomaly detection in background

which can be modeled by a multi-scale random field model. The present research is also presented in [7].

In this paper we introduce a multi-scale Gaussian Markov random field (GMRF) model and a corresponding anomaly subspace detection algorithm. The proposed model is based on a multi-scale representation of the image and independent components analysis (ICA). We generate from a given image, a multi-scale representation with independent layers which are modeled as GMRFs with different sets of parameters. The detection is subsequently carried out by applying an MSD to the innovations process of the multi-scale GMRF. The MSD incorporates the available a priori information about the targets into the detection process and thus improves the detection performance. The MSD was originally developed for signal detection in subspace interference and white Gaussian noise [21]. Here, we formulate an MSD for signal detection in subspace interference and noise which follows the multi-scale GMRF model. A quantitative performance analysis with comparison to competing methods shows the advantages of the proposed method. The proposed model and algorithm are applied to detection of airplanes in simulated cloudy backgrounds; detection of sea-mines in sonar images; and detection of defects in wafer images. The results demonstrate the robustness and flexibility of the algorithm in adverse environments. The proposed detection method we propose here is based on predetermined set of filters for generating the multi-scale representation, and on an intuitive choice of signal and interference subspaces. This may limit its practicability of the proposed method when applied to real detection problems.

The structure of the paper is as follows: In Section 2, we review the GMRF model and introduce the Multi-Scale GMRF model. In Section 3, we present the anomaly subspace detection algorithm. In Section 4, we describe the implementation of the proposed algorithm. In Section 5, we analyze its performance with a comparison to competing methods. Finally, in Section 6, we demonstrate the application of the proposed algorithm to automatic target detection in simulated and real imagery.

2. Statistical model

In this section we review the GMRF model and methods for its estimation. Subsequently we introduce the multi-scale GMRF model.

2.1. The GMRF model

We assume that each image pixel can be represented as a weighted sum of its neighboring pixels and an additive innovations process (prediction error). Let Ω be the support of an image, and let $\mathbf{s} \in \Omega$ denote the indices of a pixel in the image. Let $\mathscr{R}$ be a given set of indices representing the neighborhood of a pixel (A simple example is the 4-neighbors set where $\mathscr{R} = \{(-1,0),(1,0),(0,-1),(0,1)\}$). We denote the weight coefficient of a neighbor $\mathbf{r} \in \mathscr{R}$ by $\theta(\mathbf{r})$ and the innovations process by $\varepsilon(\mathbf{s})$. Assuming an image T can be modeled as a GMRF, a pixel $T(\mathbf{s})$ in the image[1] is related to its neighboring pixels as follows:

$$T(\mathbf{s}) = \sum_{\mathbf{r} \in \mathscr{R}} \theta(\mathbf{r})T(\mathbf{s}+\mathbf{r}) + \varepsilon(\mathbf{s}). \tag{1}$$

Let $\rho^2 = E\{\varepsilon^2(\mathbf{s})\}$ denote the variance of the innovations process. Woods [25] showed that the innovations process is spatially correlated with covariance given by:

$$E\{\varepsilon(\mathbf{s})\varepsilon(\mathbf{s}+\mathbf{r})\} = \begin{cases} \rho^2 & \text{if } \mathbf{r} = (0,0), \\ -\theta(\mathbf{r})\rho^2 & \text{if } \mathbf{r} \in N, \\ 0 & \text{otherwise.} \end{cases} \tag{2}$$

Kashyap and Chellappa [13] showed that the correlation structure imposes symmetry on the neighborhood set. That is, $\mathbf{r} \in \mathscr{R}$ implies $-\mathbf{r} \in \mathscr{R}$ and $\theta(\mathbf{r}) = \theta(-\mathbf{r})$.

In most detection problems, the background clutter model is unknown and therefore should be estimated. Various methods for model estimation were developed over the years, e.g., [11,13,23,22,26]. A computationally efficient method for the GMRF model estimation is the least squares method, described in details in Hazel [11]. Let vec($\cdot$) denote the column stack ordering of an image chip. Let the column stack ordering of the

---

[1] For simplicity, we assume $T(\mathbf{s})$ is not in the boundaries of the image, i.e. $\forall \mathbf{r} \in \mathscr{R}, (\mathbf{s}+\mathbf{r}) \in \Omega$.

neighborhood of $T(\mathbf{s})$ be denoted by $\mathbf{g}(\mathbf{s})$:

$$\mathbf{g}(\mathbf{s}) = \text{vec}[T(\mathbf{s}+\mathbf{r}), \mathbf{r} \in \mathscr{R}] \tag{3}$$

and let

$$\boldsymbol{\theta} = \text{vec}[\theta(\mathbf{r}), \mathbf{r} \in \mathscr{R}]. \tag{4}$$

Hazel [11] showed that the least squares estimates for $\boldsymbol{\theta}$ and ρ^2 are given by

$$\widehat{\boldsymbol{\theta}} = \left[\sum_{\mathbf{s}\in\Omega} \mathbf{g}(\mathbf{s})\mathbf{g}(\mathbf{s})^{\mathrm{T}}\right]^{-1} \left[\sum_{\mathbf{s}\in\Omega} T(\mathbf{s})\mathbf{g}(\mathbf{s})\right], \tag{5}$$

$$\widehat{\rho^2} = \frac{1}{|\Omega|} \sum_{\mathbf{s}\in\Omega} \left(T(\mathbf{s}) - \widehat{\boldsymbol{\theta}}^{\mathrm{T}}\mathbf{g}(\mathbf{s})\right)^2, \tag{6}$$

where $^{\mathrm{T}}$ denotes transpose.

2.2. The multi-scale GMRF model

Let $Y(\mathbf{s})$ denote an image, and let $\mathscr{G} = \{G_1, G_2, \ldots, G_n\}$ denote a given set of multi-scale spatially invariant filters (e.g. scaling and wavelet filters). We generate from the image a multi-scale image, $\mathbf{Y}$, by applying the filters to the image Y and concatenating the results in the third dimension:

$$Y_i = Y * G_i, \quad i = 1, \ldots, n, \tag{7}$$

$$\mathbf{Y}(\mathbf{s}) = [Y_1(\mathbf{s}), Y_2(\mathbf{s}), \ldots, Y_n(\mathbf{s})], \tag{8}$$

where $*$ denotes two-dimensional convolution. The result $\mathbf{Y}$ is a three-dimensional representation of the image, thus each pixel is now transformed to a vector. The Karhunen–Loéve transform (KLT) can be applied to $\mathbf{Y}(\mathbf{s})$, for generating a multi-scale image, $\mathbf{T}(\mathbf{s})$, with independent layers. $\mathbf{T}(\mathbf{s})$ has p layers representing the top p independent components of $\mathbf{Y}(\mathbf{s})$. Let K denote a matrix whose columns are the top p eigen vectors of the covariance matrix of $\mathbf{Y}(\mathbf{s})$. $\mathbf{T}(\mathbf{s})$ is then given by

$$\mathbf{T}(\mathbf{s}) = K^{\mathrm{T}}\mathbf{Y}(\mathbf{s}). \tag{9}$$

We assume that there is a set of filters, $\mathscr{G}$, such that each image layer, $\mathbf{T}_\ell(\mathbf{s})$, can be modeled as a GMRF with a different set of parameters. We denote the weight coefficient estimated for neighbor $\mathbf{r} \in \mathscr{R}$, and for the ℓth layer of $\mathbf{T}(\mathbf{s})$ by $\theta_\ell(\mathbf{r})$, and the innovations process of the ℓth layer by $\varepsilon_\ell(\mathbf{s})$. $\mathbf{T}(\mathbf{s})$ is then given by the following equation:

$$\mathbf{T}(\mathbf{s}) = \sum_{\mathbf{r}\in\mathscr{R}} \Theta_{\mathbf{r}}\mathbf{T}(\mathbf{s}+\mathbf{r}) + \boldsymbol{\varepsilon}(\mathbf{s}), \tag{10}$$

where Θ_r is the following diagonal matrix:

$$\Theta_r = \text{diag}(\theta_1(\mathbf{r}), \theta_2(\mathbf{r}), \ldots, \theta_p(\mathbf{r})) \tag{11}$$

and $\boldsymbol{\varepsilon}(\mathbf{s})$ is a vector of the innovations in pixel $\mathbf{s}$ in the different layers of $\mathbf{T}(\mathbf{s})$:

$$\boldsymbol{\varepsilon}(\mathbf{s}) = [\varepsilon_1(\mathbf{s}), \varepsilon_2(\mathbf{s}), \ldots, \varepsilon_p(\mathbf{s})]^{\mathrm{T}}. \tag{12}$$

The estimation of the model parameters for each layer, is carried out using the method described in Section 2.1. Subsequently, we can estimate the innovations process by:

$$\widehat{\boldsymbol{\varepsilon}}(\mathbf{s}) = \mathbf{T}(\mathbf{s}) - \sum_{\mathbf{r}\in\mathscr{R}} \widehat{\Theta_r}\mathbf{T}(\mathbf{s}+\mathbf{r}). \tag{13}$$

3. Anomaly detection

In this section, we introduce an anomaly subspace detection method based on a matched subspace detector and the multi-scale GMRF model introduced in the previous section.

Scharf and Friedlander [21] formulated a MSD for the general problem of detecting subspace signals in subspace interference and additive white Gaussian noise. Here, the anomaly detection is based on a statistical model which better describes the background clutter. We formulate a modified MSD for the detection of subspace signals in subspace interference and additive noise, which follows the multi-scale GMRF model.

Let $\{\mathbf{h}_j | j = 1, \ldots, u\}$ and $\{\mathbf{s}_k | k = 1, \ldots, v\}$ denote two sets of image chips, which span the signal and interference subspaces of image Y, respectively. The image chips are all of the same size: $N_x \times N_y$ pixels, which is usually much larger than the size of the neighborhood $\mathscr{R}$. It should be large enough for containing shapes which span the signal and interference subspaces.

We assume that image Y contains mainly noise, which follows the multi-scale GMRF model, and that the target and interference signals are rare. Let $\mathscr{D}_p$ denote an operator which generates the prediction error, $\widehat{\boldsymbol{\varepsilon}}(\mathbf{s})$, of the multi-scale GMRF model with p independent components. $\mathscr{D}_p$ is

defined by using (7), (9), and (13), as follows:

$$\widehat{\boldsymbol{\varepsilon}}(\mathbf{s}) = [\widehat{\varepsilon}_1(\mathbf{s}), \widehat{\varepsilon}_2(\mathbf{s}), \ldots, \widehat{\varepsilon}_p(\mathbf{s})]^\mathrm{T}$$
$$= K^\mathrm{T}\mathbf{Y}(\mathbf{s}) - \sum_{\mathbf{r}\in\mathscr{R}} \boldsymbol{\Theta}_r K^\mathrm{T}\mathbf{Y}(\mathbf{s}+\mathbf{r}) \triangleq \mathscr{D}_p Y(\mathbf{s}). \quad (14)$$

Let $\mathbf{n}_\ell(\mathbf{s})$ denote the column stack ordering of an $N_x \times N_y$ pixels image-chip of $\widehat{\varepsilon}_\ell$ around $\mathbf{s}$:

$$\mathbf{n}_\ell(\mathbf{s}) = \mathrm{vec}(\{\widehat{\varepsilon}_\ell(\mathbf{t}) | \mathbf{t} \in [N_x \times N_y$$
$$\text{image chip around } \mathbf{s}]\}). \quad (15)$$

We define H_ℓ and S_ℓ as follows:

$$H_\ell = [\mathrm{vec}([\mathscr{D}_p\mathbf{h}_1]_\ell) \ \mathrm{vec}([\mathscr{D}_p\mathbf{h}_2]_\ell) \ \ldots \ \mathrm{vec}([\mathscr{D}_p\mathbf{h}_u]_\ell)],$$
$$S_\ell = [\mathrm{vec}([\mathscr{D}_p\mathbf{s}_1]_\ell) \ \mathrm{vec}([\mathscr{D}_p\mathbf{s}_2]_\ell) \ \ldots \ \mathrm{vec}([\mathscr{D}_p\mathbf{s}_v]_\ell)], \quad (16)$$

where $[\cdot]_\ell$ denotes the ℓth layer of the three-dimensional data.

Let $\langle H_\ell \rangle$ denote the signal subspace, spanned by the columns of matrix H_ℓ and let $\langle S_\ell \rangle$ denote the interference subspace, spanned by the columns of matrix S_ℓ. We denote the additive noise by $\mathbf{b}_\ell$. The problem is to determine whether the sample vector $\mathbf{n}_\ell$ contains a target signal. The target signal $\mathbf{x}_\ell$ can be described as a linear combination of the columns of H_ℓ i.e., $\mathbf{x}_\ell = H_\ell\boldsymbol{\psi}_\ell$, where $\boldsymbol{\psi}_\ell$ is a vector of coefficients. The interference signal is described similarly, using the matrix S_ℓ and the coefficients vector $\boldsymbol{\phi}_\ell$. Considering the detection problem, we define two hypotheses, H_0 and H_1 which indicate, respectively, absence and presence of target signal in the vector $\mathbf{n}_\ell$:

$$H_0 : \mathbf{n}_\ell = S_\ell\boldsymbol{\phi}_\ell + \mathbf{b}_\ell,$$
$$H_1 : \mathbf{n}_\ell = H_\ell\boldsymbol{\psi}_\ell + S_\ell\boldsymbol{\phi}_\ell + \mathbf{b}_\ell. \quad (17)$$

Let P_{S_ℓ} denote the projection of a vector onto the subspace $\langle S_\ell \rangle$:

$$P_{S_\ell}\mathbf{n}_\ell(\mathbf{s}) = S_\ell(S_\ell^\mathrm{T}S_\ell)^{-1}S_\ell^\mathrm{T}\mathbf{n}_\ell(\mathbf{s}) \quad (18)$$

and let $P_{H_\ell S_\ell}$ denote the projection of a vector onto the subspace $\langle H_\ell S_\ell \rangle$, spanned by the columns of the concatenated matrix $[H_\ell \ S_\ell]$. The maximum likelihood estimates of the additive noise vector, $\mathbf{b}_\ell$, under H_0 and under H_1 are denoted by $\widehat{\mathbf{b}}_{H_0}^\ell$ and $\widehat{\mathbf{b}}_{H_1}^\ell$, respectively. These estimates are obtained by subtracting from $\mathbf{n}_\ell$ the components which lie in the signal and interference subspaces as follows:

$$\widehat{\mathbf{b}}_{H_0}^\ell = (I - P_{S_\ell})\mathbf{n}_\ell,$$
$$\widehat{\mathbf{b}}_{H_1}^\ell = (I - P_{H_\ell S_\ell})\mathbf{n}_\ell, \quad (19)$$

$\mathbf{b}_\ell$ is the innovations process of a GMRF and therefore is normally distributed with zero mean. We denote the covariance matrix of $\mathbf{b}_\ell$ by $\rho_\ell^2\Phi_\ell$, where ρ_ℓ^2 is the variance of $\mathbf{b}_\ell$. $\rho_\ell^2\Phi_\ell$ is obtained by using (2).

The detection problem can be formulated as a GLRT between H_0 and H_1. The log-likelihood ratio, L_ℓ, calculated based on the ℓth layer of the innovations process is given by

$$L_\ell(\mathbf{s}) = 2 \ln\left[\frac{Pr(\mathbf{b}_\ell(\mathbf{s})|H_0)}{Pr(\mathbf{b}_\ell(\mathbf{s})|H_1)}\right]$$

$$= 2 \ln\left[\frac{\exp\left(\frac{[\Phi_\ell^{-1/2}\widehat{\mathbf{b}}_{H_0}^\ell(\mathbf{s})]^2}{2\rho_\ell^2}\right)}{\exp\left(\frac{[\Phi_\ell^{-1/2}\widehat{\mathbf{b}}_{H_1}^\ell(\mathbf{s})]^2}{2\rho_\ell^2}\right)}\right]$$

$$= \frac{1}{\rho_\ell^2}[\|\Phi_\ell^{-1/2}\widehat{\mathbf{b}}_{H_0}^\ell(\mathbf{s})\|_2^2 - \|\Phi_\ell^{-1/2}\widehat{\mathbf{b}}_{H_1}^\ell(\mathbf{s})\|_2^2]. \quad (20)$$

The log-likelihood ratio, based on p layers of the innovations process is given by $L(\mathbf{s}) = \sum_{\ell=1}^p L_\ell(\mathbf{s})$ as follows:

$$L(\mathbf{s}) = \sum_{\ell=1}^p \frac{1}{\rho_\ell^2}[\|\Phi_\ell^{-1/2}\widehat{\mathbf{b}}_{H_0}^\ell(\mathbf{s})\|_2^2 - \|\Phi_\ell^{-1/2}\widehat{\mathbf{b}}_{H_1}^\ell(\mathbf{s})\|_2^2]$$
$$= \sum_{\ell=1}^p \frac{1}{\rho_\ell^2}[\Phi_\ell^{-1/2}\mathbf{n}_\ell(\mathbf{s})]^\mathrm{T}(P_{H_\ell S_\ell} - P_{S_\ell})$$
$$\times [\Phi_\ell^{-1/2}\mathbf{n}_\ell(\mathbf{s})]. \quad (21)$$

The signal-to-noise ratio (SNR) is the ratio between the signal and the noise in terms of intensity. We define the SNR as the second power of the ratio between the signal, which do not lie in the interference subspace, and the standard deviation of the noise, as follows:

$$\mathrm{SNR} = \sum_{l=1}^p \frac{1}{\rho_\ell^2} \mathbf{x}_\ell^\mathrm{T}[I - P_{\widetilde{S_\ell}}]\mathbf{x}_\ell. \quad (22)$$

Let u denote the rank of the signal subspace and let $q = up$. L is the sum of squared independent

normally distributed variables and therefore is chi-square distributed with q degrees of freedom, as follows:

$$L \sim \begin{cases} \chi_q^2(0) & \text{under } H_0 \\ \chi_q^2(\text{SNR}) & \text{under } H_1. \end{cases} \tag{23}$$

Under the hypothesis H_1, the non-centrality parameter of the chi-square distribution of L is equal to the SNR. The decision rule

$$L \underset{H_1}{\overset{H_0}{\gtrless}} \eta \tag{24}$$

yields false-alarm and detection probabilities, which are, respectively, given by

$$P_{\text{FA}} = 1 - P[\chi_q^2(0) \leqslant \eta], \tag{25}$$

$$P_{\text{D}} = 1 - P[\chi_q^2(\text{SNR}) \leqslant \eta]. \tag{26}$$

4. Implementation

In this section, we describe the implementation of the proposed anomaly detection algorithm. Fig. 1 presents a flow chart with the main steps of the algorithm:

(1) *Generation of a multi-scale representation*: The image Y is filtered by a set of spatial filters, $\mathscr{G}$, using (7), in order to create its multi-scale representation, **Y**.
(2) *Independent components analysis*: The Karhunen–Loéve transform is applied to the vectors of the multi-scale representation, **Y**, using (9). The result is a multi-scale representation, **T**, with independent layers.
(3) *Estimation of the innovations process*: The GMRF parameters set is separately estimated for each layer of **T**. The sample innovations, $\widehat{\varepsilon}_\ell(\mathbf{s})$, are calculated for each layer, ℓ, of **T** using (14) and the estimated parameters.
(4) *Matched subspace detector*: S_ℓ and H_ℓ are calculated using (16). A matched subspace detector is formed and the log-likelihood ratio, L, is calculated for each pixel using (21).
(5) *Decision rule (thresholding)*: The decision rule given in (24) is applied to the log-likelihood ratio, L, in order to determine whether a pixel **s**
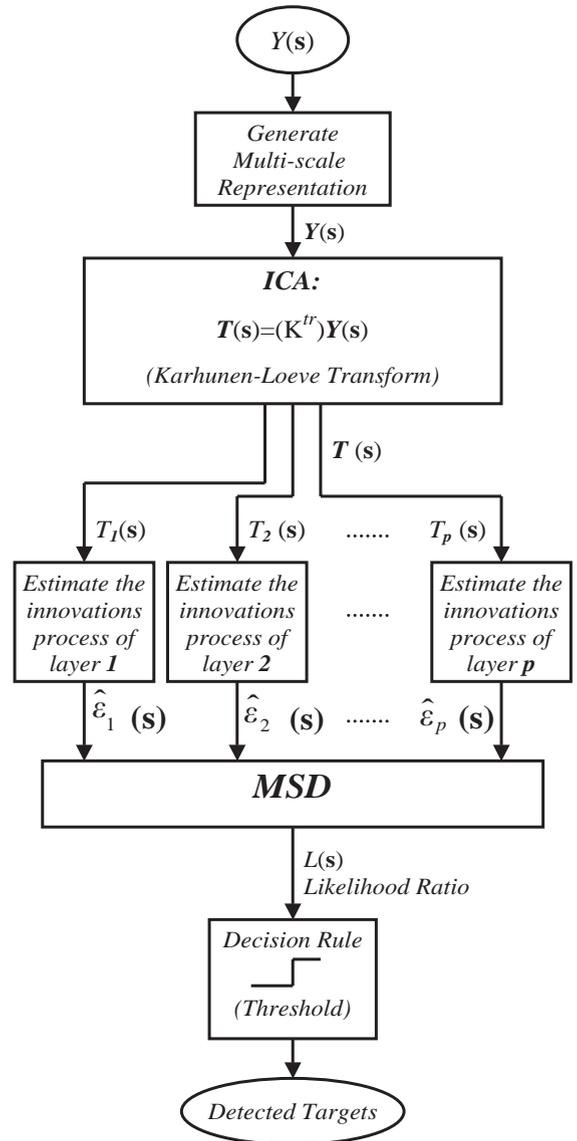

Fig. 1. Flow chart of the proposed algorithm.

belongs to a target. The threshold, η, is determined by the admissible false alarm rate (FAR) using (25).

The computational complexity of the proposed algorithm is a function of the size of the image ($M_x \times M_y$), the rank of the subspace in which the signal and interference lie ($N_x \times N_y$), and the number of independent components p employed

for the detection. The computational complexity of the multi-scale representation generation is $O(nN_xN_yM_xM_y)$ where n is the number of multi-scale filters. Applying the KLT to the multi-scale representation of the image using the covariance matrix of the data is: $O(N_x^2N_y^2M_xM_y + N_x^3N_y^3)$ [6]. Using the singular value decomposition (SVD) - based approach, reduces the computational complexity of the KLT to $O(N_x^2N_y^2M_xM_y)$ [12]. The estimation of the innovations process is $O(|\mathcal{R}|M_xM_y)$ and the MSD is $O(M_xM_yN_xN_yp)$. Thus, the total computational complexity of the proposed algorithm is $O(N_x^2N_y^2M_xM_y + N_xN_yM_xM_yn + |\mathcal{R}|M_xM_y)$.

5. Performance analysis

In this section we analyze the performance of the proposed algorithm. We investigate the receiver operating characteristics (ROC) of the algorithm with respect to different parameters. The ROC of the proposed algorithm is calculated using (22), (25), and (26). The SNR, given by (22), is a function of the target's shape and intensity, the variance of the background's innovations process and the interference subspace span. The SNR increases with the norm of **x**, the number of independent layers (p), and the angle between **x** and $\langle S \rangle$. Large background variance results in a smaller SNR and therefore, performance degradation.

Fig. 2 presents the ROC of the proposed algorithm for various SNRs. This example presents the performance of the proposed anomaly detection algorithm using three independent components ($p = 3$). The probability of false alarm (P_{FA}) and the probability of detection (P_D) are calculated using (25) and (26), respectively. Fig. 3 presents the ROC versus p given a constant target norm and background variance. The SNR and the probability of detection (P_D) improve with p. The use of more independent layers improves the detection performance due to the additional information concealed in each layer. Another factor which may influence the performance is the dimension of the interference subspace. According to (22), when the dimension of S'_ℓ
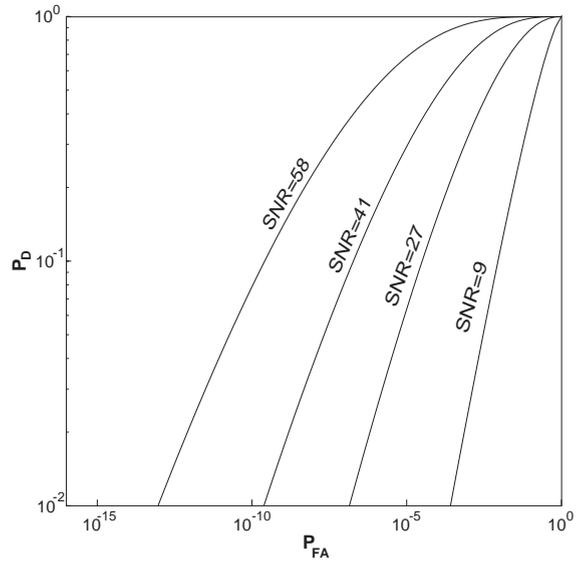

Fig. 2. An example of ROC calculated for the proposed algorithm, using three principle component ($p = 3$) and various values of SNR.
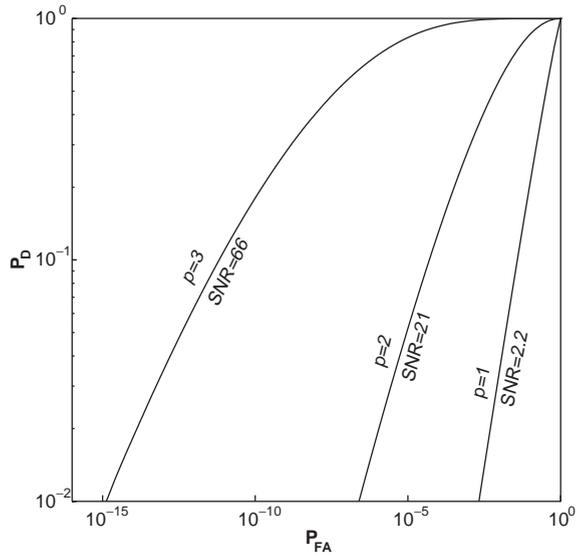

Fig. 3. An example of ROC calculated for the proposed algorithm using p independent components. Using larger number of independent components, increases the SNR and improves the performance.

decreases, the SNR is lower and the performance is reduced. In this section we refer to the proposed method as "*Proposed Method III*" and compare it

to a competing method and to other proposed methods, namely *Methods I and II*. The latter proposed methods are similar to the *Proposed Method III* except that they do not include all of its elements. We applied the competing methods to synthetic images of airplanes on cloudy backgrounds. The synthetic images are generated by the process described in Section 6.1. Fig. 4 shows the flowcharts of the different methods compared in this section:

Competing Method: We assume the image follows the GMRF model. A single hypothesis scheme is applied to the estimated innovations process of the image for the detection of regions, which appear unlikely with respect to its normal distribution [11].

Proposed Method I: We assume the image follows the conventional GMRF model rather than the multi-scale GMRF model. The MSD, proposed by Scharf and Friedlander [21], is applied to the estimated innovations process. By analyzing the performance of this method and

comparing it to *Method III* we examine the contribution of the proposed multi-scale model to the detection performance.

Proposed Method II: The multi-scale GMRF model is employed, skipping the KLT step. We assume the layers of the multi-scale representation $Y(\mathbf{s})$ follow the GMRF model and estimate the innovations process of each of these layers. The MSD, proposed in Section 3, is applied to the estimated innovations process. By analyzing the performance of this method we examine the significance of the KLT in the modeling process.

Proposed Method III: This method includes all the elements of the multi-scale model proposed in Section 3. We assume the image follows the proposed multi-scale GMRF model. The MSD, proposed in Section 3, is applied to the estimated innovations process.

Figs. 5 and 6 present examples in which the proposed and competing algorithms are applied to the same synthetic images of airplanes on cloudy background. Fig. 5 shows the synthetic images,
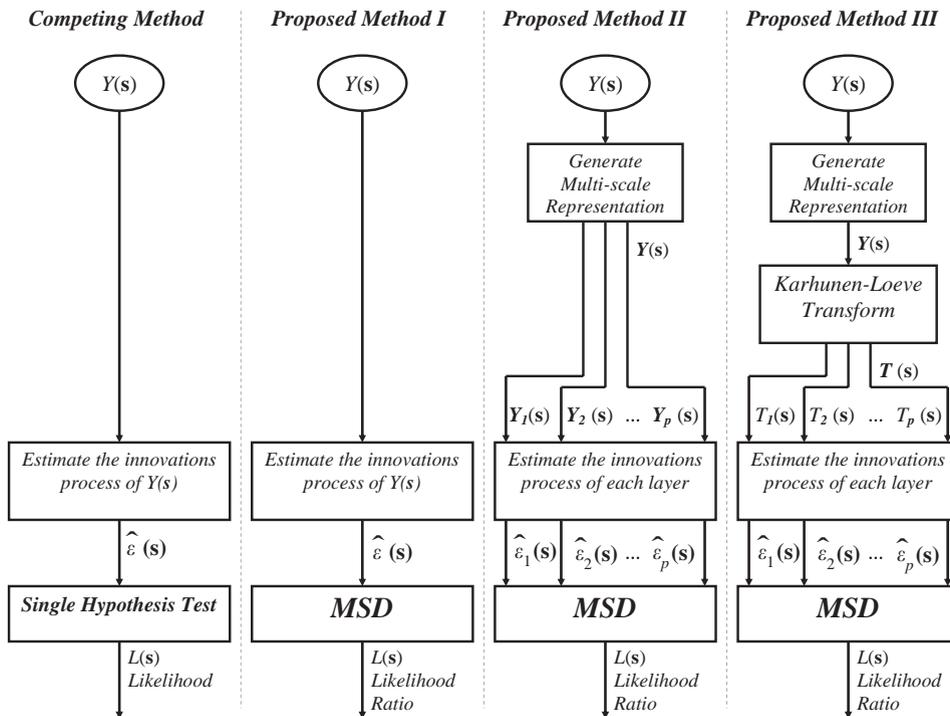

Fig. 4. Flowcharts of the compared detection methods.

generated using a mixture of three images of different periodical patterns (generated by summing up three GMRFs with three different parameters sets). The airplane is planted in the center of each image.

Figs. 6(a)–(d) present the results of applying the *Competing Method*, the *Proposed Method I*, the *Proposed Method II*, and the *Proposed Method III* to the images in Fig. 5, respectively. Fig. 6(d) shows the best detection results. The likelihood ratios are relatively low everywhere except in the target's region. The results of the *Competing Method* contain high level of background noise which does not allow the targets detection by
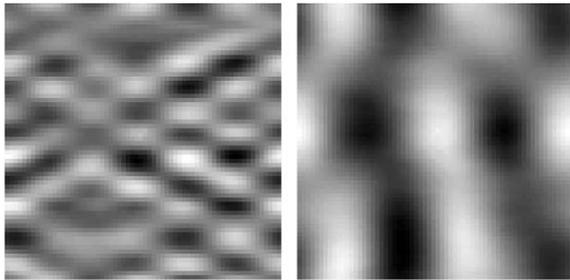
thresholding the likelihood image. The results of *Proposed Method II* contain a noisy pattern which exceeds the likelihood level in the targets region (in the center of the image). According to these examples, it seems that skipping the KLT in the modeling process, significantly reduces the performance obtainable by using the *Proposed Method III*.

Fig. 7 presents the ROC, analytically calculated for synthetic images of an airplane on cloudy sky. The ROC curves reflect the performance of *Proposed Method II* (solid) compared to the performance of *Proposed Method I* (dashed). The images, for which the ROC's where calculated, are similar to the right example presented in Fig. 5. The only difference between the images is in the SNR.

The SNRs for which the ROCs where drawn are summarized in Table 1. The table specifies four different cases of background variances and target norms (L-infinity norms of the targets image). The SNRs obtained by *Proposed Method III*, which is based on the multi-scale GMRF model, are higher than those obtained by *Proposed Method I*, which is based on a conventional GMRF model, and *Proposed Method II*, which is based on a modification of the multi-scale GMRF model.

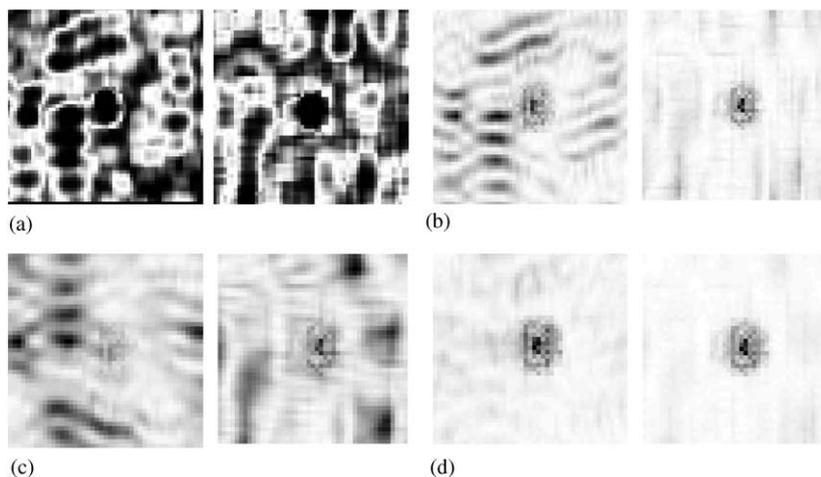Fig. 5. Synthetic images containing cloudy background and an airplane target in their centers.

Fig. 6. A comparison between detection methods. (a) Results of the *Competing Method* applied to the images in Fig. 5; (b) results of *Proposed Method I* applied to the images in Fig. 5; (c) results of *Proposed Method II* applied to the images in Fig. 5; (d) results of *Proposed Method III* applied to the images in Fig. 5. The images in (d) seems to have the lowest false alarm rate (FAR).
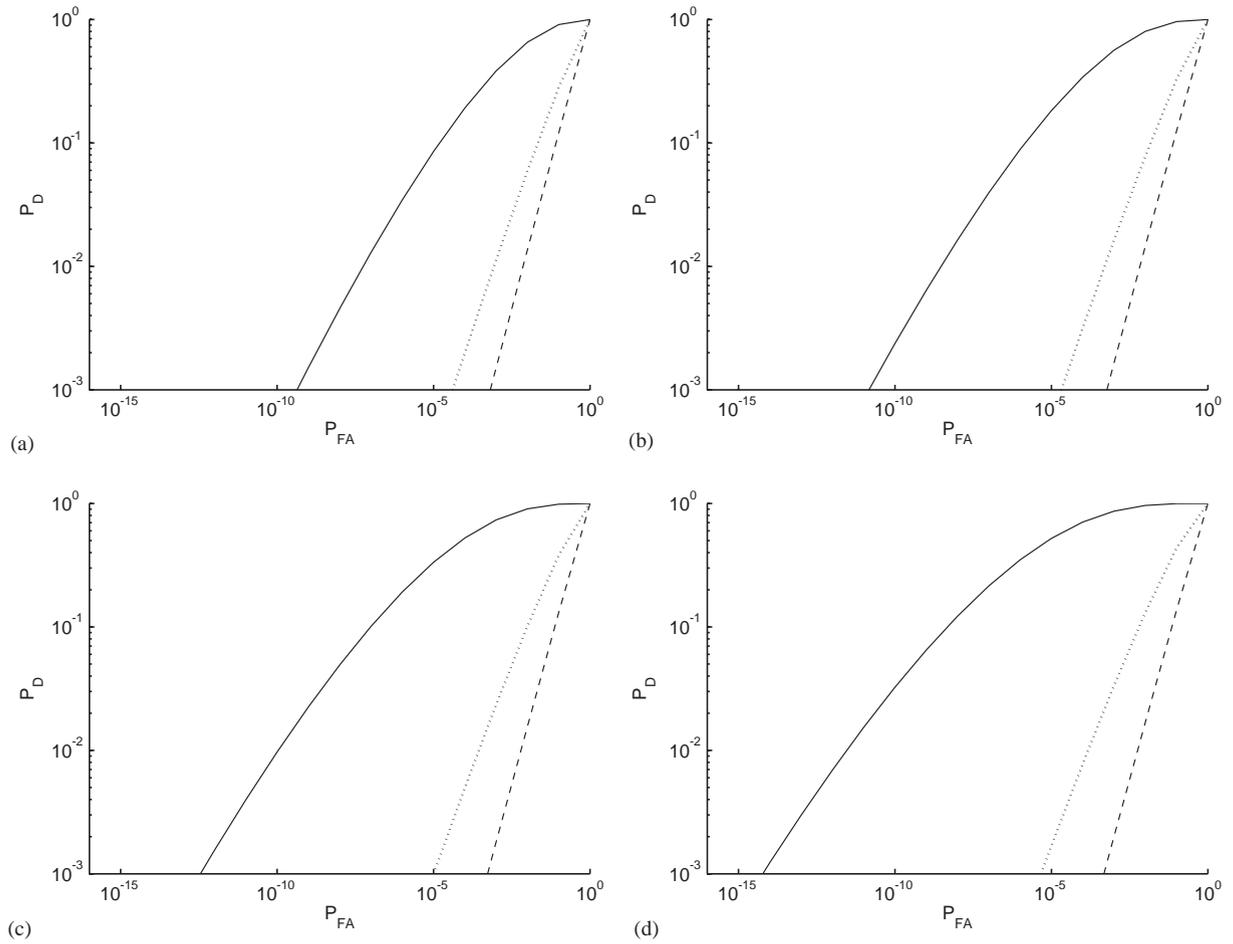
Fig. 7. Performance of the anomaly detection based on *Proposed Method III* (solid), *Proposed Method II* (dashed), and *Proposed Method I* (dotted). (a)–(d) correspond to different parameter settings as specified in Table 1.

Table 1
Properties of the different cases for which the ROC curves in Fig. 7 were drawn. The SNR calculated for *Proposed Method III* is significantly higher than the SNR calculated for the other methods

Case	Background variance	Target norm	SNR[dB]		
			Proposed Method I	Proposed Method II	Proposed Method III
(a)	188	1.3	2.8	−0.5	7.3
(b)	188	1.4	3.2	0	7.7
(c)	188	1.5	3.6	0.4	8.1
(d)	188	1.7	4.0	0.8	8.5

6. Experimental results

In this section, we present the results of applying the proposed model and algorithm to synthetic and real images from different sources. The algorithm is applied to: (1) simulated images of airplanes on cloudy background; (2) sonar images of sea-mines on sea-bottom background; and (3) detection of defects in wafer images. The different examples and applications demonstrate the robustness and flexibility of the algorithm.

6.1. Synthetic images

The synthetic examples presented in this subsection contain airplanes on cloudy background. The synthetic cloudy background is generated using random images which follow the GMRF model. These random images are obtained by using a formulation of the GMRF model in terms of white noise. Let $T(\mathbf{s})$ be an image of $M_x \times M_y$ pixels which follows the GMRF model, let $\mathscr{F}$ be the discrete Fourier transform (DFT) operator, and let $\mathbf{w} = (w_1, w_2)$ be the two-dimensional indices of the data in the frequency domain. Then the DFT of $T(\mathbf{s})$ is as follows [13]:

$$\mathscr{F}\{T\}(\mathbf{w})$$
$$= \frac{\rho \mathscr{F}\{v(\mathbf{s})\}}{\sqrt{1 - 2\sum_{\mathbf{r} \in \mathscr{R}_h} \theta(\mathbf{r})\cos(2\pi[r_1 w_1/M_x + r_2 w_2/M_y])}}, \quad (27)$$

where $\{v(\mathbf{s})|\mathbf{s}\}$ are independent and identically distributed (IID) Gaussian random variables, with zero mean and unit variance, $\mathscr{R}_h$ is half of the symmetric neighborhood $\mathscr{R}$, and $\mathbf{r} = (r_1, r_2)$. For the model to exist and be stable, the following expression must be true for every $\mathbf{w}$ in the support of the image:

$$1 - 2 \sum_{\mathbf{r} \in \mathscr{R}_h} \theta(\mathbf{r}) \cos\left(2\pi\left[\frac{r_1 w_1}{M_x} + \frac{r_2 w_2}{M_y}\right]\right) > 0. \quad (28)$$

From (27), the procedure for synthetic generation of random fields obeying this model is evident. Further details can be found in [13].

The synthetic examples of airplanes on cloudy background are generated as follows:

(1) Three random images are generated based on the GMRF model. Each image is obtained by using (27) with different sets of parameters.
(2) A weighted sum of the three images is calculated. The result contains several periodical patterns with different period lengths.
(3) A small airplane image is planted in the background image in a random position and orientation.

The results of this procedure contain mixtures of periodical patterns with different period lengths. This procedure does not describe an accurate synthesis of images which follow the multi-scale GMRF model. The process only claims to generate images that may be better described by the multi-scale GMRF model rather than the conventional GMRF model. The results demonstrate that the effective SNR achieved by the MSD under the multi-scale GMRF model assumption (*Proposed Method III*) is higher than the SNR achieved under the conventional GMRF model assumption (*Proposed Method I*).

Fig. 8 shows examples of synthetic images generated as described above. A multi-scale representation of each image is obtained by applying undecimated wavelet transform with two scale levels to the image. Accordingly, the layers of the multi-scale representation are the result of convolving the image with the wavelet basis images. We employ a signal subspace that is constructed from the span of four image chips of 11×11 pixels. The image chips contain bar shapes in different orientations: $0°, 45°, 90°$, and $135°$ which resemble the fuselage of airplane targets. Fig. 9 shows the log-likelihood ratio (in grayscale), calculated using (20). Black regions denote high log-likelihood ratio. The target detection is carried out by thresholding the likelihood images. The threshold is determined by the predefined admissible level of FAR. The detected targets are marked by circles (in Fig. 9). This example demonstrates the robustness of the algorithm in presence of different patterns of background. The image chips which span the signal subspace (target
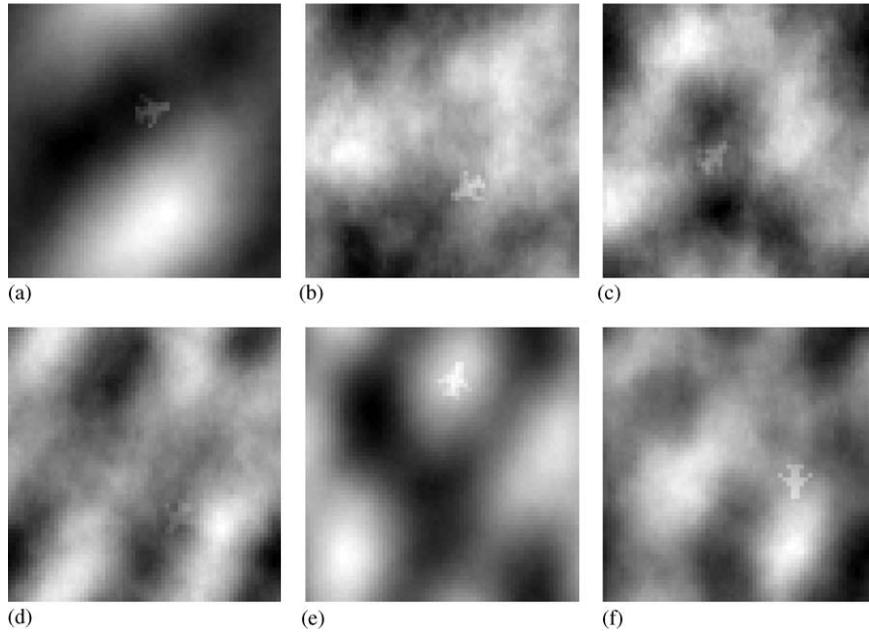
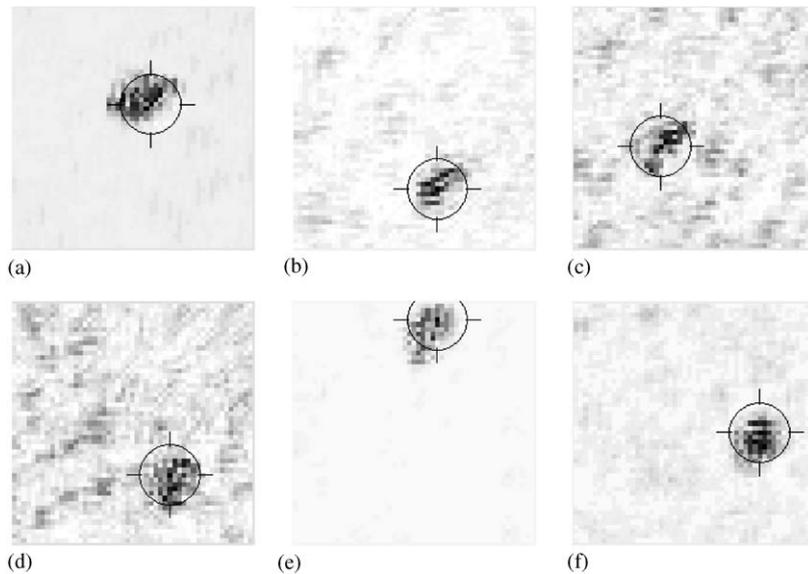Fig. 8. Synthetic images of cloudy sky with airplane images planted in random places and orientations.

Fig. 9. Results of anomaly detection applied to the images in Fig. 8. The gray-scale represents the degree of local anomality around a given pixel. The circles indicate regions where the local anomality is above a predetermined threshold.

subspace) are simple and generally do not require detailed information about the targets.

Figs. 10 and 11 show an example of target detection using the proposed algorithm with three

independent components ($p = 3$). Fig. 10 shows a synthetic image of cloudy sky with an airplane in its middle. The airplane is unnoticeable by a human viewer due to its weak signature. Figs. 11(a)–(c)
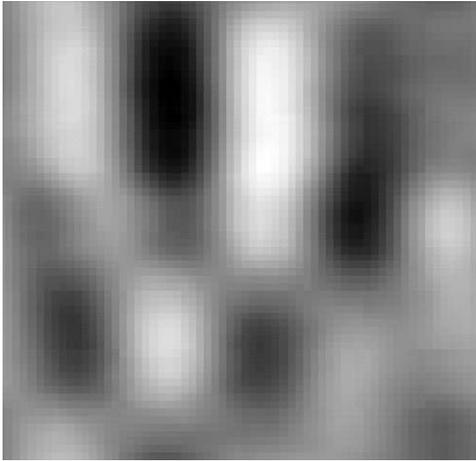
Fig. 10. A synthetic image of cloudy sky with an airplane in its middle. The airplane is unnoticeable by a human viewer due to its weak signature.

show the images of the three top independent components generated by the algorithm (as detailed in Section 2). The target is clearly revealed in the third independent component. Fig. 11(d) shows the likelihood ratio calculated by the proposed algorithm. This image, unlike the images of the independent components, lacks the background patterns, which are rejected by the innovations noise and likelihood ratio calculations. Thus, the target is more clearly revealed.

6.2. Sea-Mine sonar images

The proposed method is demonstrated on real images from a database of sea-mine sonar images. A sea-mine appears in the sonar images as a bar shaped object-highlight accompanied by a
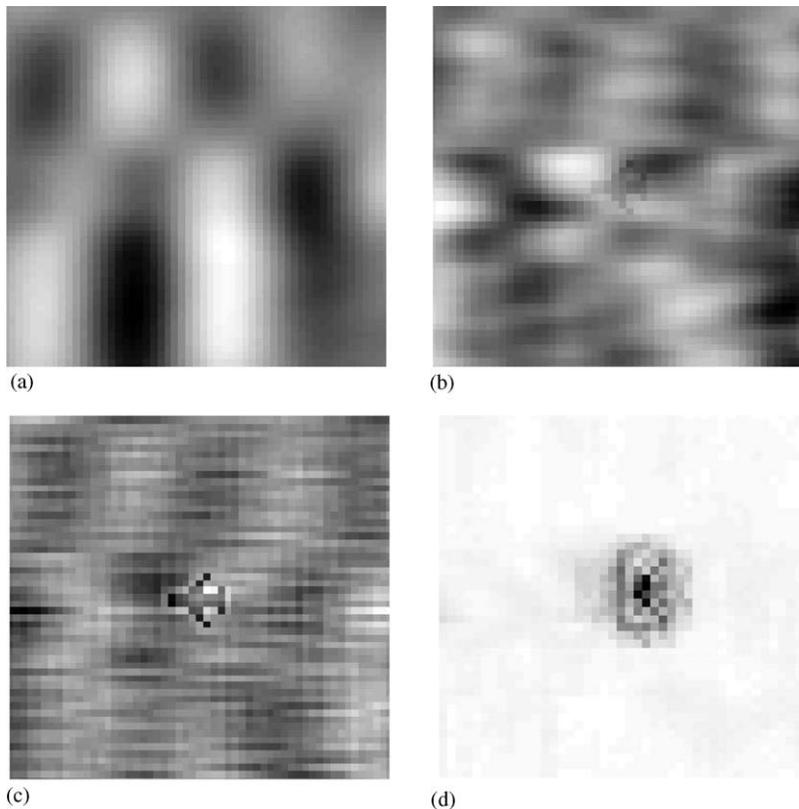

Fig. 11. Anomaly detection applied to the image in Fig. 10. (a) First, (b) second, and (c) third independent components. (d) Likelihood ratio calculated by the proposed algorithm.

shadow which represents the hiding of the seabottom-reverberation by the sea-mine [19]. Mignotte and Collet [18] presented 3-class Markovian segmentation method for the detection of sea-mines in sonar images. The sea-mine images were segmented to three regions: echo, shadow, and sea-bottom reverberation areas, based on different MRF models, estimated for the different classes. Dobeck et al. [4] implemented a matched filter, K-nearest neighbor neural network classifier, and a discriminatory filter classifier to detect such mine-like objects in sonar images. The classification process employs up to 45 features for every possible mine-like object. The detection in [4] is based on a large collection of mine-like objects signatures. In the example presented here, no real signature examples are used for defining the signal subspace. Fig. 12 shows six sonar images. Each image contains one sea-mine on highly cluttered seabottom background. The background patterns are diverse. Figs. 12(a)–(e) contain relatively slow changing backgrounds while Fig. 12(f) contains background with a dominant periodical pattern. The sea-mine's highlight in

Fig. 12(f) is unnoticeable while its shadow clearly appears as a dark region. The proposed method is applied to these images for detecting sea-mines. The multi-scale representations of the images are generated by applying undecimated wavelet transform with three scale levels to the images. The signal subspace is formed from the span of four image-chips of highlighted bars with dark shadows, in different orientations. The result of the proposed anomaly detection, applied to the sonar images, is shown in Fig. 13. The sea-mine in Fig. 12(f) is detected despite the absence of sea-mine highlight, due to its dominant shadow. The lower right circle in Fig. 13(c) marks a false alarm. This false alarm might result from a mine-like highlight in the background pattern.

The detection results presented here, demonstrate the capability of the proposed model and algorithm to cope with variety of background clutter patterns, using the same filters set and signal subspace. All the sea-mines in these examples are detected. The false alarm in Fig. 13(c) may be prevented by a more specific definition of the signal subspace.
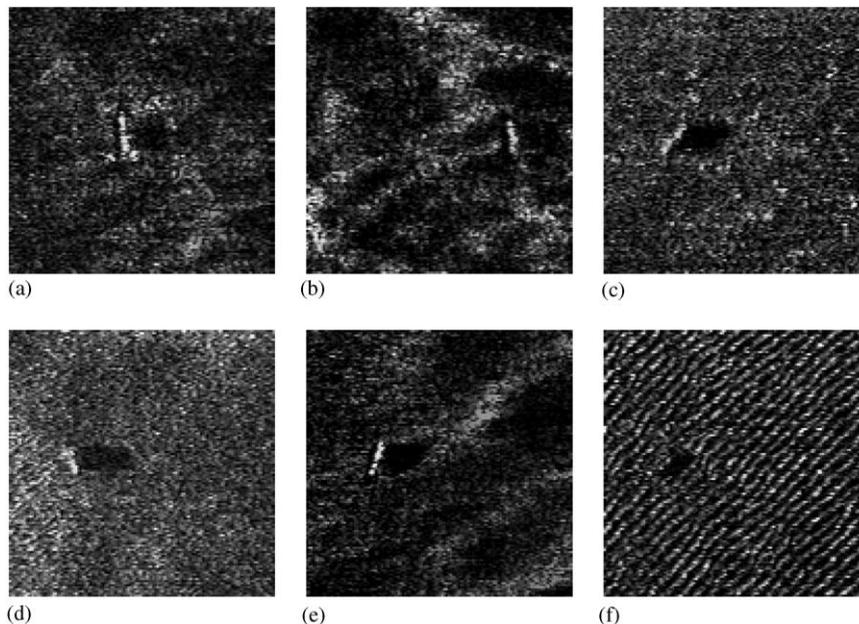

Fig. 12. Examples of sea-mine sonar images: sea-mines appear in the sonar images as a bar shaped object-highlight accompanied by a shadow which represents the hiding of seabottom-reverberation by the sea-mine [19].
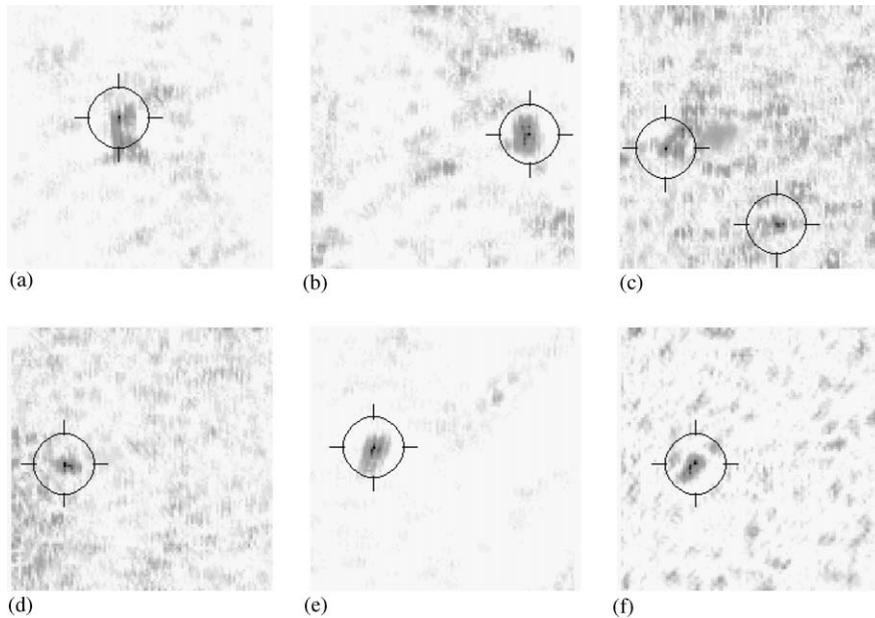
Fig. 13. Results of the anomaly detection applied to the images in Fig. 12. The sea-mines are detected by thresholding the gray-scale values which represent the degree of local anomaly around a given pixel.
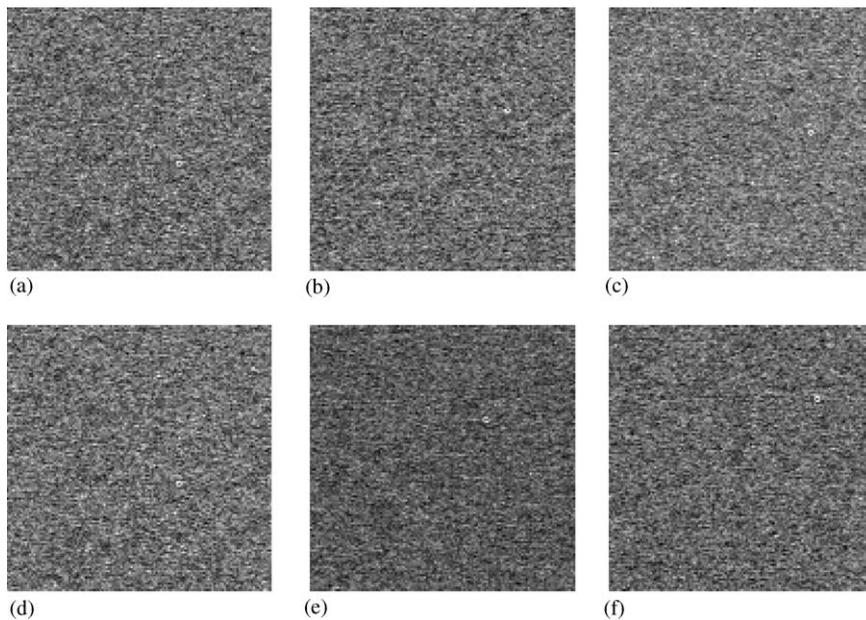

Fig. 14. Example of wafer images. The 128×128 images include small round defects of about 3×3 pixels.

6.3. Wafers images

The proposed algorithm is applied to detection of defects in wafers images for quality assurance.

Fig. 14 shows examples of wafer images. Each image contains a defect whose diameter is smaller than three pixels. The MSD is set to detect circles of three pixels diameter and linear shapes of three
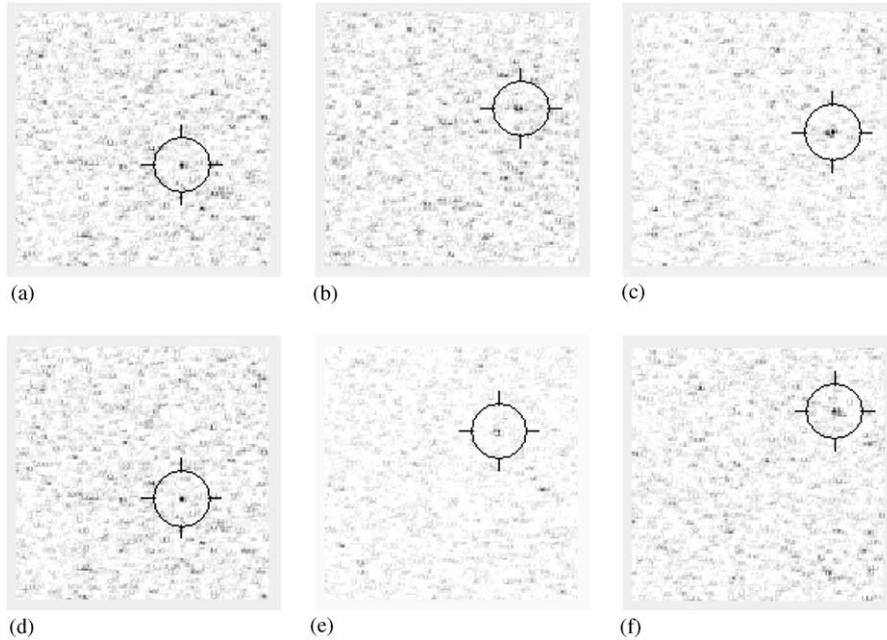
Fig. 15. Results of the anomaly detection applied to the images in Fig. 14.

pixels length. The multi-scale representation is generated in the same way as described in the synthetic example. The likelihood images and the detected targets are presented in Fig. 15. The results are less impressive than those obtained in the previous applications. However, we are still able to detect the defects with a manageable rate of false alarms. The cause of the performance degradation may be explained by the low correlation of the background patterns. Images with weakly correlated patterns are not well described by the multi-scale GMRF model.

7. Conclusion

We have introduced a multi-scale GMRF model and a corresponding anomaly subspace detection algorithm. The proposed model is based on a multi-scale representation of the image and ICA. We assumed that there is a set of scaling filters, for which, each independent component of the multi-scale representation of the image follows a GMRF model. Under this assumption, each image layer is modeled as a GMRF. The detection is then carried

out by applying MSD to the innovations process of the estimated multi-scale GMRF. The MSD incorporates the available a priori information about the targets into the detection process and thus potentially improves the detection performance. The performance of the algorithm was demonstrated with application to automatic target detection in synthetic images, side-scan sonar data and wafer images. The results show the capability of the proposed model and algorithm to cope with variety of targets and background clutter patterns. Performance analysis was carried out by investigating the influence of different parameters on the detection performance, and comparing the performance of the proposed method to those of competing methods. The analysis as well as the experimental results demonstrate the advantages of the proposed method.

The model and algorithm presented here are based on given subspaces of signal and interference. Interactive definition of the signal and interference subspaces may limit the practicability of the proposed method when applied to real detection problems. The examples we present have demonstrated the robustness of the algorithm,

based on an intuitive choice of these subspaces. A rigorous procedure which defines the signal and interference subspaces may improve the performance of the proposed algorithm and enable its adjustment to different detection problems.

References

[1] M.G. Bello, A random-field model-based algorithm for anomalous complex image pixel detection, IEEE Trans. Image Process. 1 (2) (April 1992) 186–196.

[2] J. Bennet, A. Khotanzad, Modeling textured images using generalized long correlation models, IEEE Trans. Pattern Anal. Mach. Intell. 20 (12) (December 1998) 1365–1370.

[3] R. Chellappa, R.L. Kashyap, Texture synthesis using 2-d noncausal autoregressive models, IEEE Trans. Acoust. Speech Signal Process. ASSP-33 (1) (February 1985) 194–203.

[4] G.J. Dobeck, J.C. Hyland, L. Smedley, Automated detection/classification of sea mines in sonar imagery, in: Proceedings of SPIE, vol. 3079, Orlando, FL, April 1997, pp. 90–110.

[5] K.B. Eom, Long-correlation image models for texture with circular and elliptical correlation structures, IEEE Trans. Image Process. 10 (7) (July 2001) 1047–1055.

[6] D. Fradkin, D. Madigan, Experiments with random projections for machine learning, in: Proceedings of the Ninth ACM SIGKDD International Conference on Knowledge Discovery and Data Mining, ACM Press, New York, NY, USA, 2003, pp. 517–522.

[7] A. Goldman, Anomaly subspace detection based on a multi-scale markov random field model, Master's Thesis, Technion, Technion City, Haifa, Israel, 32000, August 2004.

[8] A. Goldman, I. Cohen, Anomaly detection based on an iterative local statistics approach, in: Proceedings of the 23rd IEEE Convention of the Electrical and Electronic Engineers in Israel, Tel-Aviv, Israel, September 2004, IEEE, pp. 440–443.

[9] A. Goldman, I. Cohen, Anomaly subspace detection based on a multi-scale markov random field model, in: Proceedings of the 23rd IEEE Convention of the Electrical and Electronic Engineers in Israel, Tel-Aviv, Israel, September 2004, IEEE, pp. 444–447.

[10] A. Goldman, I. Cohen, Anomaly detection based on an iterative local statistics approach, Signal Process 84 (7) (2004) 1225–1229.

[11] G.G. Hazel, Multivariate gaussian GMRF for multi-spectral scene segmentation and anomaly detection, IEEE Trans. Geosci. Remote Sensing 38 (3) (May 2000) 1199–1211.

[12] K.V.R. Kanth, D. Agrawal, A. El Abbadi, A. Singh, Dimensionality reduction for similarity searching in dynamic databases, Technical Report 1998–10, University of California, May 1998.

[13] R.L. Kashyap, R. Chellappa, Estimation and choice of neighbors in spatial-interaction models of images, IEEE Trans. Inform. Theory IT-29 (1) (January 1983) 60–72.

[14] R.L. Kashyap, P.M. Lapsa, Sythesis and estimation of random fields using long correlation models, IEEE Trans. Pattern Anal. Mach. Intell. 6 (6) (November 1984) 800–809.

[15] C. Kervrann, F. Heitz, A Markov random field model-based approach to unsupervised texture segmentation using local and global spatial statistics, IEEE Trans. Image Process. 4 (6) (June 1995) 856–862.

[16] P. Lévi, A special problem of brownian motion, and a general theory of gaussian random functions, in: Third Berkeley Symposium Mathematical Statistics and Probability, vol. 2, California Press, Berkeley California, 1956.

[17] M. Markou, S. Singh, Novelty detection: a review - part 1: statistical approaches, Signal Processing 83 (12) (July 2003) 2481–2497.

[18] M. Mignotte, C. Collet, Three-class markovian segmentation of high-resolution sonal images, Comput. Vision Image Understand. 76 (3) (December 1999) 191–204.

[19] S. Reed, Y. Petillot, J. Bell, An automatic approach to the detection and extraction of mine features in sidescan sonar, IEEE J. Ocean. Eng. 28 (1) (January 2003) 90–105.

[20] A. Sarkar, M.K. Biswas, K.M.S. Sharma, A simple unsupervised GMRF model based image segmentation approach, IEEE Trans. Image Process. 9 (5) (May 2000) 801–811.

[21] L.L. Scharf, B. Friedlander, Matched subspace detectors, IEEE Trans. Signal Process. 42 (8) (August 1994) 2146–2156.

[22] S.M. Schweizer, J.M.F. Moura, Hyperspectral imagery: clutter adaption in anomaly detection, IEEE Trans. Inform. Theory 46 (5) (August 2000) 1855–1871.

[23] S.M. Schweizer, J.M.F. Moura, Efficient detection in hyperspectral imagery, IEEE Trans. Image Process. 10 (4) (April 2001) 584–597.

[24] A. Speis, G. Healey, Feature extraction for texture discrimination via random field models with random spatial interaction, IEEE Trans. Image Process. 5 (4) (April 1996) 635–645.

[25] J.W. Woods, Two-dimensional discrete Markovian fields, IEEE Trans. Inform. Theory IT-18 (2) (March 1972) 101–109.

[26] P. Zhao, J. Litva, Consistency of modified LS estimation method for identifying 2-D noncausal SAR model parameters, IEEE Trans. Automat. Control 40 (2) (February 1995) 316–320.